BALKAN JOURNAL OF ELECTRICAL & COMPUTER ENGINEERING, Vol. 13, No. 3, September 2025
Research Article

Modeling of an Electro-Hydraulic System for Wave Generation in a Wave Channel

Batin Demircan, Tugce Yaren, Ersin Akyuz, Sabri Bicakci

***Abstract*—This paper presents a black-box mathematical model of the electrohydraulic system controlling the wave generation structure in a wave channel under various operating conditions. For the position control of the system, NI-CRIO 9074 hardware and LabVIEW software were used. Open-loop position control experiments of the hydraulic cylinder were conducted using stimulus signals with different initial positions (0, 120, and 240 mm) and amplitudes. Data were recorded for different sampling times: 1 ms, 2 ms, 5 ms, and 10 ms. The recorded data were processed using the System Identification Toolbox (SIT) in MATLAB, and system models were developed in both continuous and discrete time domains using transfer function, state space, and AutoRegressive with eXogenous input (ARX) models. These models were compared and analyzed based on their fit rates to the training and test data. Among the system models with high compliance rates, the top three models were selected for further comparison using an additional test dataset. Based on this evaluation, the transfer function model (120 mm initial condition and 1 ms sampling time) type was identified as the best-performing model. This model was successfully integrated into the real-time control study, achieving effective controller performance.**

Index Terms—**Wave channel, Electro-hydraulic system, Hydraulic control, System identification, Black-box.**

Batın Demircan, Department of Electronics and Automation, Balıkesir Vocational School, Balıkesir University, Balıkesir, Turkey,
Institue of Science, Department of Electrical and Electronics Engineering, Balıkesir University, Balıkesir, Turkey,
Renewable Energy Research, Application and Development Center, Balıkesir University, Balıkesir, Turkey,
(e-mail: batin.demircan@balikesir.edu.tr).
https://orcid.org/0000-0002-0765-458X

Tugce Yaren, Department of Electrical and Electronics Engineering, Faculty of Engineering, Balıkesir University, Balıkesir, Turkey,
Renewable Energy Research, Application and Development Center, Balıkesir University, Balıkesir, Turkey,
(e-mail: tugce.yaren@balikesir.edu.tr).
https://orcid.org/0000-0001-9937-3111

Ersin Akyuz, Department of Electrical and Electronics Engineering, Faculty of Engineering, Balıkesir University, Balıkesir, Turkey,
Renewable Energy Research, Application and Development Center, Balıkesir University, Balıkesir, Turkey,
(e-mail: eakyuz@balikesir.edu.tr).
https://orcid.org/0000-0001-9786-3221

Sabri Bicakci, Department of Electrical and Electronics Engineering, Faculty of Engineering, Balıkesir University, Balıkesir, Turkey,
Renewable Energy Research, Application and Development Center, Balıkesir University, Balıkesir, Turkey,
(e-mail: sbicakci@balikesir.edu.tr).
https://orcid.org/0000-0002-2334-8515
Manuscript received Jan 18, 2025; accepted Apr 22, 2025.
DOI: 10.17694/bajece.1622216

I. INTRODUCTION

WAVE CHANNEL SYSTEMS are critically important in many engineering and research fields, such as interaction with coastal structures, wave energy, and flood and tsunami modeling [1-3]. These systems enhance the accuracy of experimental studies by generating water waves in specific forms. Wave generation is typically carried out using flap, plunger, or piston-type mechanical systems, and these mechanisms are driven by technologies such as electric motors, servo systems, pneumatic actuators, and electrohydraulic systems (EHS) [4, 5].

EHS, with its high power-to-weight ratio and rapid response capabilities, stands out by enabling the generation of complex waveforms in wave channel applications. However, their complex structures, arising from nonlinear dynamics, time-varying parameters, and susceptibility to external disturbances, necessitate accurate dynamics modeling and the development of effective control strategies [6].

System identification techniques play a critical role in the modeling processes of EHSs. These techniques enable the development of models that accurately represent the system's dynamics using various mathematical approaches such as transfer function (TF), state space (SS), and AutoRegressive with eXogenous input (ARX) models with external inputs, leveraging experimental data [7-10]. Each modeling method offers different advantages in analyzing system dynamics and designing effective control strategies. While transfer functions and state-space models are more traditional approaches, the ARX model offers a data-driven alternative that can be particularly useful in scenarios where system dynamics are complex and cannot be easily captured by physical models.

The choice of modeling technique depends on the specific requirements of the EHS application, as well as the desired accuracy, computational efficiency, and the complexity of the system dynamics. Each method contributes to a deeper understanding of system behavior and facilitates the development of effective control strategies. In the literature, numerous studies have been conducted using various methods and approaches to better understand the complex dynamics of EHSs and to develop accurate system models. Rahmat et al. used the MATLAB System Identification Toolbox (SIT) to derive an ARX model of the EHS and designed a PID controller tuned with the Ziegler-Nichols method based on the obtained model [8]. Similarly, Das et al. utilized artificial neural networks to model the nonlinear dynamics of an electrohydraulic actuator (EHA) system and validated the model with experimental data [11]. Salleh et al. also used SIT to identify an ARX model of the EHA system and reported that, during the model validation phase, the predicted model demonstrated high accuracy in representing the actual system behavior, achieving a best fit of 94.88% [12].

The Recursive Least Squares (RLS) method is one of the approaches used for system identification of EHSs. Ghazali et al. modeled the EHA system with time-varying parameters using the system identification method and derived a linear discrete-time model. The model parameters were estimated using the RLS algorithm [13]. Furthermore, the use of nonlinear state-space models, as explored by Yan et al., enables a more comprehensive representation of system behavior under varying operating conditions and significantly enhances the accuracy of the identified models [14].

Black-box modeling techniques have gained increasing importance in the modeling of EHSs due to their capability to represent complex system dynamics without requiring detailed knowledge of underlying physical processes. These approaches rely solely on input-output data to develop mathematical models that can predict system behavior under various operating conditions [15]. Jin and Wang highlighted that black-box methods, such as artificial neural networks and fuzzy systems, can effectively capture the dynamics of hydraulic cylinders by fitting models to experimental data, thereby addressing the inherent modeling uncertainties present in hydraulic systems [16]. This capability is particularly important in EHS applications, where inherent nonlinearities and varying operational conditions often complicate traditional modeling approaches.

Mitov et al. successfully achieved control performance by analyzing the robustness of an electro-hydraulic steering control system using a black-box model [17]. The implementation of advanced control strategies, such as Model Predictive Control (MPC) and Linear Quadratic Regulator (LQR), largely depends on accurate system identification. By comparing the performance of these controllers, Mitov et al. demonstrated that the effectiveness of control strategies is significantly influenced by the quality of the underlying system model obtained through identification techniques [18].

Recent advances in electrohydraulic systems have highlighted the critical need for accurate and efficient modeling approaches, particularly under varying operating conditions. While traditional white-box models rely heavily on detailed physical parameters, recent studies have demonstrated the growing importance of black-box and data-driven techniques for capturing system dynamics with limited sensor data [19, 20]. For instance, Schwarz and Lohmann [21] proposed a robust identification method based solely on pressure signals, enabling effective modeling even in sensor-constrained mobile hydraulic systems. Similarly, energy-focused investigations by He et al. [22] emphasized the role of pump-controlled architectures in improving system efficiency, while Han et al. [23] introduced deep learning methods to predict complex nonlinearities such as friction in hydraulic actuators. In a related effort, Kim et al. [24] demonstrated that neural network inverse models could outperform traditional adaptive control in force control of hydraulic actuators, highlighting the limitations of physical models under uncertain dynamics. Likewise, Jiang et al. [25] proposed a neural network-based adaptive disturbance rejection strategy that integrates model reference control with nonlinear hydraulic models, showing increased robustness under high nonlinearities. Dindorf [26] further contributed to this domain by introducing a discrete incremental hydraulic positioning system using binary valves, which achieves accurate sensorless step positioning based on dynamic modeling and simulation. Building upon these developments, this study presents a black-box modeling framework for an electrohydraulic wave-generation system, emphasizing model accuracy, experimental validation, and integration into real-time position control.

In this study, the dynamics of the EHS, illustrated in the schematic diagram in Fig. 1, were examined using a black-box modeling approach applied to the wave generation mechanism located in a 24x1x1 m laboratory-scale wave channel at the Department of Civil Engineering, Faculty of Engineering, Balıkesir University. Experiments were conducted by applying stimulus signals with varying initial positions (0 mm, 120 mm, and 240 mm) and amplitude values, and the corresponding system responses were recorded. The collected data were processed using the SIT, and models were obtained in transfer function (TF), state-space (SS), and ARX structures. The prediction performance of these models was evaluated under different sampling times (1 ms, 2 ms, 5 ms, and 10 ms) for each initial condition. The model fit (FIT) ratios of the TF, SS, and ARX models were assessed for all initial positions. Furthermore, the models developed using training datasets were tested on validation datasets at different time scales.

This study presents a comprehensive analysis of the dynamics of a wave-generating mechanisms under varying initial conditions and sampling times, contributing to the modeling process of EHSs. The findings lay a significant foundation for improving the control performance of electrohydraulic systems in wave channel applications. The main contributions of this study are outlined as follows:

- Experimental modeling of an electrohydraulic flap-type wave generator system under different initial positions and amplitude levels.
- Development and comparison of TF, SS, and ARX models using the SIT, based on a black-box modeling approach.
- Evaluation of model accuracy across various sampling times to support the design of effective control strategies.

The structure of this paper is organized as follows: the section "Materials and Methods" details the EHS, the methodology for conducting experiments, and the development of transfer function, state-space, and ARX models using the SIT. The section "Results" discusses the validation of the obtained models under various operating conditions and their comparative analysis. The section "Conclusion" provides the final conclusions and future work.

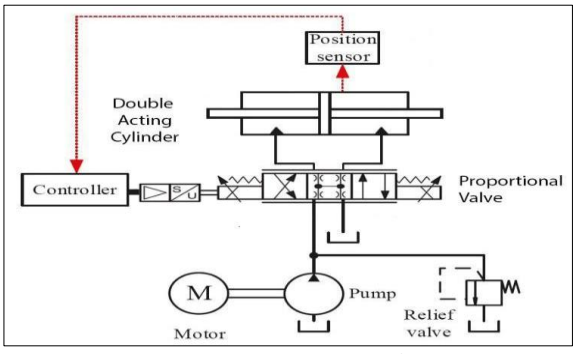

Fig. 1. Schematic diagram of EHS

II. Material and Methods

A. System Overview and Modeling

The EHS used in this study consists of a hydraulic cylinder and a hydraulic pump unit, as shown in Fig. 2a. The hydraulic cylinder is a double-acting, double-rod servo cylinder, while the hydraulic pump unit is equipped with a proportional

directional control valve, a hydraulic power supply, and safety components. This system is central to the experimental setup, as shown in Fig. 2b, and plays a key role in generating and controlling the wave dynamics, as shown in Fig. 2c.

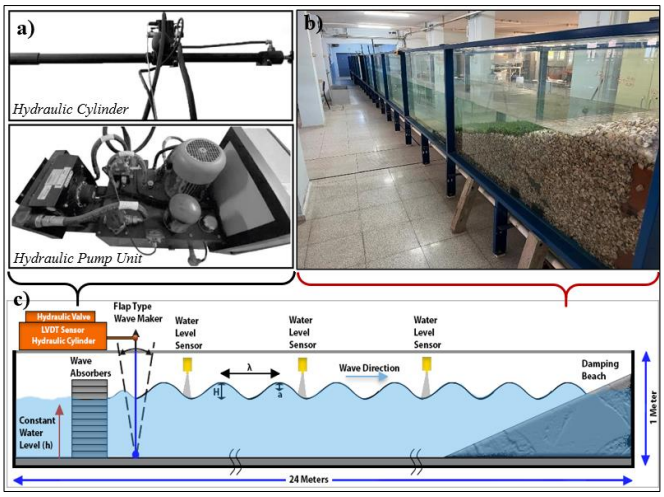

Fig. 2. (a) Hydraulic cylinder and pump unit (EHS), (b) physical wave channel system, (c) general structure of the wave channel.

The NI-CRIO 9074 packaged controller (PAC) used for EHS position control is operated by the user via LabVIEW software running on a Windows platform. Table 1 presents the hardware specifications of the NI-CRIO 9074 PAC [27].

TABLE I
NI-CRIO 9074 PAC SPECIFICATIONS

FEATURE	SPEC
Processor	400MHz Freescale MPC2500
Memory	128 MB
Flash Memory	256 MB
I/O Module Slots	8 hot-swappable C Series module

To provide a clearer understanding of the architecture within the experimental setup, a detailed block diagram of the system is shown in Fig. 3.The diagram illustrates the interactions between the hardware components—including the NI-CRIO-9074 controller, LabVIEW interface, hydraulic valve, servo cylinder, and the flap-type wave maker—along with their electrical, mechanical, and hydraulic connections. This structure enabled real-time data acquisition and control during the experiments.

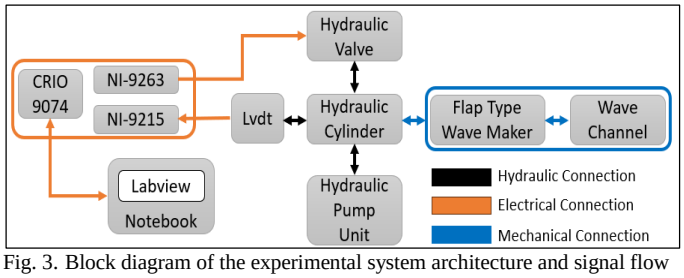

Fig. 3. Block diagram of the experimental system architecture and signal flow

The hydraulic servo cylinder used in the wave channel is custom-made, designed to handle a frequency of 0.625 Hz at a 300 mm stroke value and a +/- 150 amplitude. The general structure of the servo cylinder is shown in Fig. 4. Since the servo cylinder is double-ended and double-acting, the chamber volumes are equal when the cylinder is at the 350 mm position.

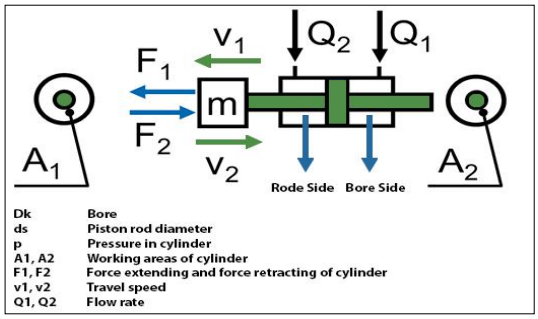

Fig. 4. Hydraulic servo cylinder.

The servo cylinder consists of two main parts: the bore side and the rod side. Because the cylinder is symmetrical, the areas on both sides are equal. The area and force generated by the servo cylinder are calculated using the following equations:

$$A = \frac{\pi}{4}(D^2 - d^2) \quad (1)$$

$$F = P.A \quad (2)$$

where D is the piston diameter, d is the rod diameter, P is the hydraulic pressure, A is the piston area, and F is the generated hydraulic force. The cylinder volume, the time required for piston travel, and the volumetric flow rate are calculated based on piston area and stroke length (L), as follows:

$$V = A.L \quad (3)$$

$$t = \frac{L}{v} \quad (4)$$

$$Q = A.v \quad (5)$$

where v is the average piston velocity, V is the cylinder volume. The design criteria for the cylinder include a piston diameter of 50mm, a rod diameter of 28mm, a stroke length of 700mm, an oil flow rate of 48 lpm, and a fixed operating pressure of 30 bar. The results of these calculations are provided in Table 2.

TABLE II
CALCULATED HYDRAULIC SERVO CYLINDER PARAMETERS

SPEC	VALUE
Area (cm^2)	13.4774
Volume (l)	0.9434
Force (kN)	4.0432
Time (sec)	1.1792
Velocity (m/s)	0.5935
Outflow (lpm)	63.930

TABLE III
HYDRAULIC PROPORTIONAL DIRECTIONAL VALVE PARAMETERS

SPEC	VALUE
Nominal Voltage	24 VDC
Absorbed Power	70 W
Maximum Current	2.6 A
Current Signal	-10/+10 V
Duty Cycle	4-20 mA
Max operating pressure -P-A-B	100%
Max operating pressure -T port	350 bar
Nominal flow with Δ10bar P-T	210 bar

The proportional directional valve (PDV) used in the EHS is the Duplomatic Oleodinamica DSE3J model, which receives control signals in the range of ±10 V. It governs the flow of

hydraulic fluid to the servo cylinder, thereby enabling position control within the 0–700 mm range. The NI-CRIO 9074 PAC communicates with this valve via analog output modules. The fluid used has a density of 0.869 kg/L and a kinematic viscosity of 46 cSt. The specifications of the PDV used in the system are summarized in Table 3.

Although all hydraulic components in the wave channel system can be modeled mathematically, the nonlinear characteristics of the hydraulic system—such as pressure-dependent behavior, temperature sensitivity, and fluid dynamics—make the derivation of a complete analytical model highly challenging. Therefore, only essential mathematical formulations for the hydraulic servo cylinder and its associated flow dynamics are considered. The PDV ports—P (connected to the pump), T (connected to the tank), and A/B (connected to the two sides of the cylinder)—allow bidirectional control of the cylinder position, as illustrated in Fig. 5.

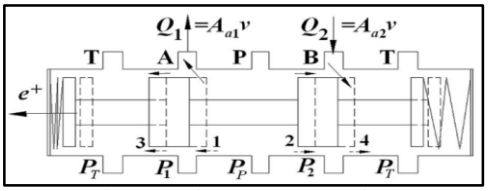

Fig. 5. Schematic of the PDV flow at neutral and for positive excitation.

The motion of the hydraulic piston can be generally described by Newton's second law, which states that the net force acting on a moving mass equals the sum of inertial, damping, and spring forces. This relationship is expressed in the classical form:

$$F = m\ddot{x} + b\dot{x} + kx \tag{6}$$

However, in electro-hydraulic systems, the driving force is not applied directly but is instead generated by hydraulic pressure acting on the piston surfaces. By considering the effective pressure forces on both sides of the piston, along with the return stiffness and friction force F_f, the dynamic equation of motion can be reformulated as:

$$\dot{y} = v\,,\ \dot{v} = \frac{P_1 A_{a1} - P_2 A_{a2} - k_y - F_f}{m_a} \tag{7}$$

where P denotes the pressures acting on the left and right chambers of the piston, k is the spring stiffness coefficient, y represents the piston displacement, and m_a is the equivalent moving mass of the system.

To fully describe the behavior of the electro-hydraulic system, it is essential to model not only the piston dynamics but also the flow dynamics through the PDV, since the control input directly affects the pressure applied to the cylinder chambers. The valve dynamics determine how the control signal e influences the hydraulic flow rates entering and leaving the piston chambers.

The relationship between the control input, pressure differences, and flow rates is governed by nonlinear orifice equations. For positive excitation ($e \geq 0$), piston extension occurs, and flow is directed through valve ports P–A and B–T. The corresponding flow rates are expressed as:

$$Q_1 = A_{a1}v = \left(C_1 e\sqrt{(P_p - P_1)} + C_1\sqrt{(P_p - P_1)}\right) - C_1\sqrt{(P_1 - P_T)} \tag{8}$$

$$Q_2 = A_{a2}v = \left(C_4 e\sqrt{(P_2 - P_T)} + C_1\sqrt{(P_2 - P_T)}\right) - C_1\sqrt{(P_p - P_2)} \tag{9}$$

where the terms Q_1 and Q_2 denote the volumetric flow rates through the valve ports P–A and B–T, respectively. P_p is the pump pressure, and P_T is the tank pressure. C_1 and C_4 are dimensionless discharge coefficients representing the flow characteristics of the valve orifices. Similarly, in the case of a negative command (e < 0), the retraction of the piston can be modeled with the P−B and A−T flows.

Frictional forces are another critical component of the model and the frictional force in the system can be expressed using a static modeling approach, as:

$$F_f = F_0, \qquad |v| \leq v_0\,, \tag{10}$$

$$F_f = F_c + (F_b - F_c)\exp\{-\frac{(v - v_b)^2}{(v_s - v_b)^2}\} + a_v(v - v_0), |v| > v_0 \tag{11}$$

where F_0 represents the adhesion force; v_0 denotes the slip velocity; F_c indicates the Coulomb friction; v_s corresponds to the Stribeck velocity; and a_v represents the viscous friction coefficient. Additionally, F_b signifies the maximum limit lubrication friction, and represents the associated velocity.

The complete hydraulic power unit includes components such as safety valves, filters, and a fixed-displacement pump. The PDV controls the flow to the hydraulic cylinder based on command voltages from the NI-CRIO control system, which interacts with an analog input/output module and an LVDT sensor for real-time position feedback. Due to the inherent nonlinearity of the EHS and its sensitivity to environmental and operational variables deriving an exact white-box model is challenging. Therefore, in this study, a black-box modeling approach is adopted. System identification techniques using input-output data are employed to develop empirical models (TF, SS, ARX), which capture the dominant system dynamics under various initial conditions and sampling intervals.

B. Data Acquisition

A flap-type wave generator was utilized in a 24 m × 1 m × 1 m wave channel to produce various wave forms, and the laboratory-scale physical setup of the wave channel system is shown in Fig. 6.

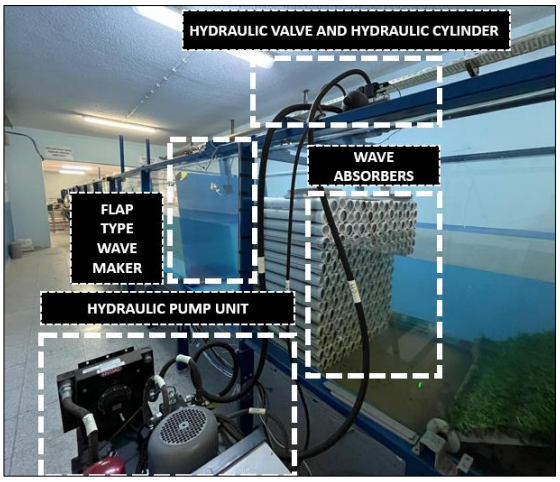

Fig. 6. Wave channel.

For the development and identification of the EHS model used in the position control of the flap-type wave generator,

both LabVIEW and MATLAB software were utilized. As illustrated in Fig. 7, the configuration includes the NI-CRIO 9074 and analog input-output modules serve as the PAC hardware. The position of the hydraulic cylinder is controlled by a proportional valve, and feedback is obtained from a 4–20 mA output LVDT sensor. The hydraulic power unit provides the required flow and pressure for system operation.

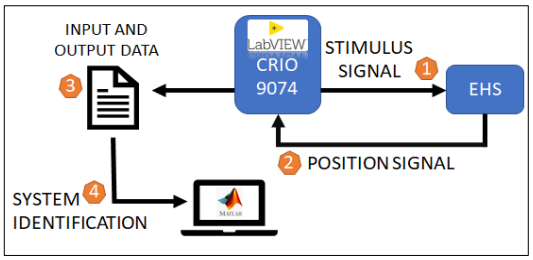

Fig. 7. EHS system identification data collection and mode generation structure.

To excite the system dynamics, stimulus signals composed of three different sinusoidal components were applied at initial positions of 0 mm, 120 mm, and 240 mm. These signals, given in Equations 12−14, were used to measure and record the position data of the hydraulic cylinder in response to these signals in real time.

$$y = 1.5(sin2\pi(0.05t)) + 0.9(sin2\pi(0.2t)) + 2.2(sin2\pi(t)) \quad (12)$$

$$y = 1.1(sin2\pi(0.05t)) + 0.9(sin2\pi(0.2t)) + 2.2(sin2\pi(t)) \quad (13)$$

$$y = 1.1(sin2\pi(0.05t)) + 0.5(sin2\pi(0.2t)) + 0.8(sin2\pi(t)) \quad (14)$$

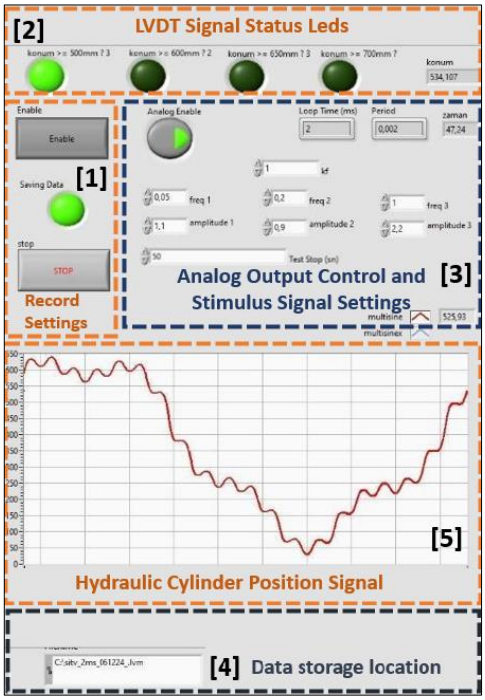

Fig. 8. EHS control software developed in Labview software.

The experimental interface, developed in LabVIEW and shown in Fig. 8, includes the following functional components: (1) start/stop control for testing, (2) LED indicators showing the real-time LVDT position, (3) configuration of stimulus signal parameters and control of the analog output, (4) file path selection for saving acquired data, and (5) real-time visualization of the cylinder position.

At each initial position, the stimulus signal was applied at four different cycle times (1 ms, 2 ms, 5 ms, and 10 ms), and the resulting position data were recorded. The collected input-output data were then transferred to MATLAB for system identification. TF, SS, and ARX models were generated using the SIT. An overview of the identification process is provided in Fig. 9.

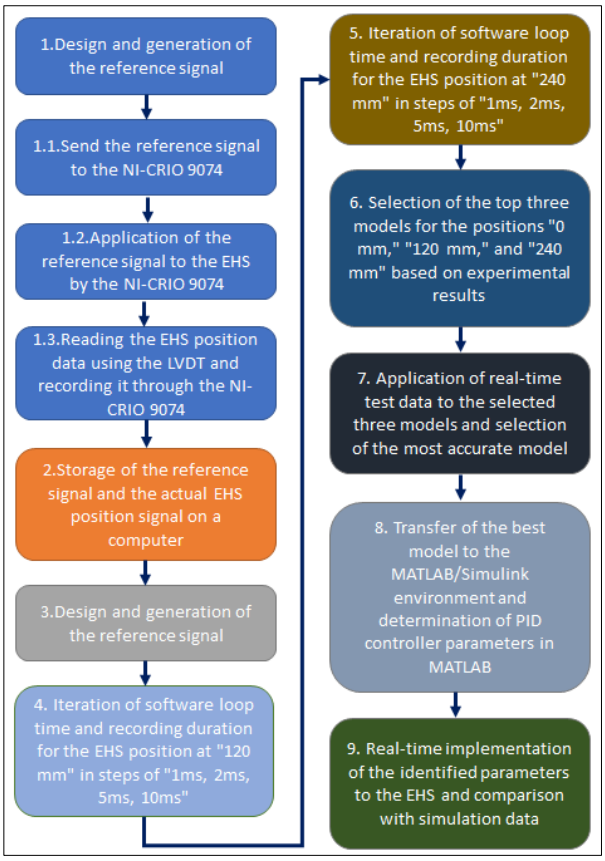

Fig. 9. EHS identification process

C. *System Identification*

System identification methods are categorized into three main approaches based on the level of system knowledge: *White-box* model method is used when the physical structure and mathematical model of the system are fully known. It is typically defined based on physical principles. *Grey-box* model approach combines theoretical and experimental methods and is employed when some parts of the system are known while the remaining parts are completed through data or estimation. *Black-box* model method is utilized when the internal structure of the system is entirely unknown. Mathematical models are developed solely based on input-output data. Instead of understanding the system dynamics, the black-box model focuses on making predictions through data-driven approaches, which is particularly advantageous for complex, nonlinear, or systems that are challenging to model physically.

The SIT enables the development of mathematical models based on input-output data of systems. It includes features for creating transfer function models, state-space models, autoregressive models (ARX, ARMAX), and nonlinear models such as Hammerstein-Wiener.

In this study, the selected models and their characteristics were chosen to analyze the dynamic behavior of the cylinder system from different perspectives and to obtain a model that

best represents the system's features. The transfer function model with three poles and two zeros directly represents the input-output relationship of the system and is useful for understanding the fundamental properties of dynamic systems. Both continuous and discrete-time representations allow accurate examination of the real system in digital control environments (discrete-time) and theoretical analysis processes (continuous-time).

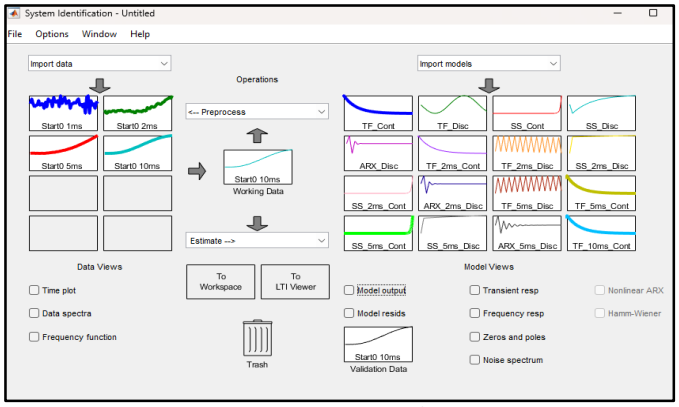

Fig. 9. Matlab SIT interface.

Second- and third-order state-space models offer a more flexible and detailed dynamic representation by directly addressing the system's state variables. Low-order state-space models are capable of representing the fundamental characteristics of the system while maintaining manageable complexity. Continuous-time and discrete-time state-space models provide a suitable framework for both the theoretical analysis of the physical system and for numerical simulations and control design. The ARX (4,4,1) and ARX (3,3,1) models are valid only for discrete-time systems and were selected due to their ability to quickly and practically model autoregressive structures. ARX models are a suitable option for rapidly predicting the linear relationship between high-frequency data and input-output. In particular, higher-order models like ARX (4,4,1) can capture more complex relationships between input and output, while lower-order models like ARX (3,3,1) provide the ability to generalize with a simpler structure. In selecting these model structures, the goal was to evaluate the linear and nonlinear dynamic characteristics of the system, compare the prediction performance of different structures, and optimize model accuracy from both theoretical and practical perspectives. This approach not only adds academic depth to the system identification process but also enhances the applicability of the obtained models in various applications.

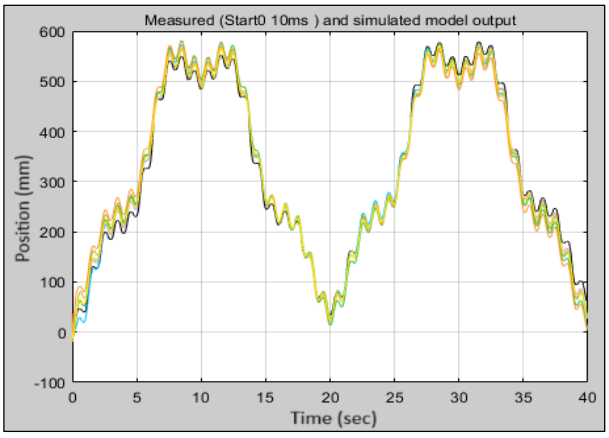

Fig. 10. Model estimation results for the training data with a 0 mm initial condition and a 10 ms sampling time (a).

In the system identification process, a distinction is made between training data and test data to evaluate the accuracy and generalization capability of the model. Training data is used to estimate the model parameters and enables the system to learn its input-output behavior. This data is selected to represent the fundamental dynamics of the system. Test data, on the other hand, is used to assess the model's performance and generalization ability. This dataset, which is not used during training, is crucial for analyzing the model's accuracy on different data sets beyond the training data. Experimental data collected from the system under 0-120-240 mm initial conditions, with four different sampling times, were sequentially imported into the SIT interface as training data, as shown in Fig. 9.

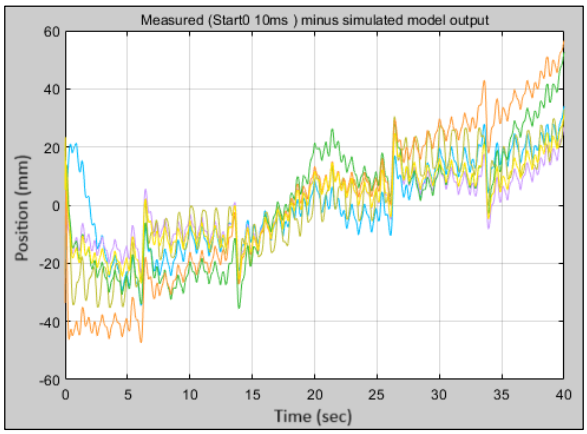

Fig. 11. Model estimation results for the training data with a 0 mm initial condition and a 10 ms sampling time (b).

In this study, the performance of the predicted models was evaluated using the best-fit ratio between the measured system output and the simulated model output. Fig. 10 and Fig.11 presents graphs illustrating the fit of the predicted models to the measured system output, using input-output data with a 10 ms sampling time as an example. Fig. 10 illustrates how accurately the predicted models replicate the system output, whereas Fig. 11 presents the error signal between the measured and simulated outputs. Fig. 10 illustrates a comparison between the measured system output and the outputs of various simulated models using input-output data sampled at 10 ms. The ARX (4,4,1) model, shown in purple, and the ARX (3,3,1) model, shown in yellow, achieved the highest fit ratios of 93.79% and 92.49%, respectively, demonstrating superior performance in capturing the system dynamics. The continuous-time transfer function model, represented in blue, yielded a fit ratio of 91.29%, while the discrete-time transfer function model, shown in green, achieved 90.19%. Both the continuous-time and discrete-time state-space models, depicted in light and dark green, exhibited fit ratios of 88.13%. The third-order discrete-time state-space model, shown in orange, had the lowest performance with a fit ratio of 83.94%. As illustrated in the graph, the ARX models—particularly those shown in purple and yellow—most accurately replicated the system behavior.

Fig. 11 illustrates the error signals between the measured system output and the outputs of various simulated models. The ARX (4,4,1) (purple, 93.79%) and ARX (3,3,1) (yellow, 92.49%) models demonstrated the best performance, exhibiting the lowest error signals throughout the time interval. These models remained closest to zero error, indicating a highly

accurate replication of the system dynamics. The continuous-time transfer function model (blue, 91.29%) and the discrete-time transfer function model (green, 90.19%) followed with moderate error magnitudes. The continuous-time and discrete-time state-space models (light green and dark green, both 88.13%) showed slightly higher error variations. The third-order discrete-time state-space model (orange, 83.94%) yielded the largest error signal, particularly in the latter stages of the simulation. The color-coded traces in Figure 11 clearly reveal that the ARX models outperformed the others in terms of both accuracy and consistency across the entire simulation period.

The ARX (4,4,1) and ARX (3,3,1) models demonstrated the best performance with fit ratios of 93.79% and 92.49%, respectively. The fit ratios for the transfer function (both continuous and discrete-time) and state-space models were calculated as 91.29%, 90.19%, 88.13%, and 83.94%, respectively. As shown in the graphs, the ARX models, in particular, successfully represented the system's dynamics with a low error signal.

III. RESULTS

A. *Identification of EHS Model*

The model prediction performance of the cylinder system for different initial conditions (0 mm, 120 mm, 240 mm) was analyzed at different sampling times (1 ms, 2 ms, 5 ms, 10 ms) and is presented in Tables 4, 5, and 6, respectively. For each initial condition, the FIT of different model structures, such as the TF, SS, and ARX models, were evaluated. Additionally, the models obtained from the training dataset were tested against validation datasets at different time scales.

According to the results obtained for the 0 mm initial condition presented in Table 3, the ARX models provided the highest fit ratios (89.47%–94.92%), particularly in discrete-time systems, and successfully represented the system's dynamic behavior. In this context, the ARX (4,4,1) model delivered the most reliable results, showing consistent performance across all sampling times (ranging from 92.5% to 94.92%). Among the TF models, the continuous-time 3-pole, 2-zero structure exhibited good performance at low sampling times (85.77%–91.29%), while the discrete-time versions, with low accuracy rates (e.g., -21.98%), failed to sufficiently represent the system's dynamics.

SS models, particularly second-order continuous-time models (88.7%–92.02%), provided satisfactory results and demonstrated a high generalization capacity during validation processes. However, the performance of third-order state-space models was lower, which is associated with the negative impact of increased model complexity on generalization capacity. Continuous-time models generally achieved higher accuracy at different sampling times, reflecting the flexibility and universal characteristics of continuous models.

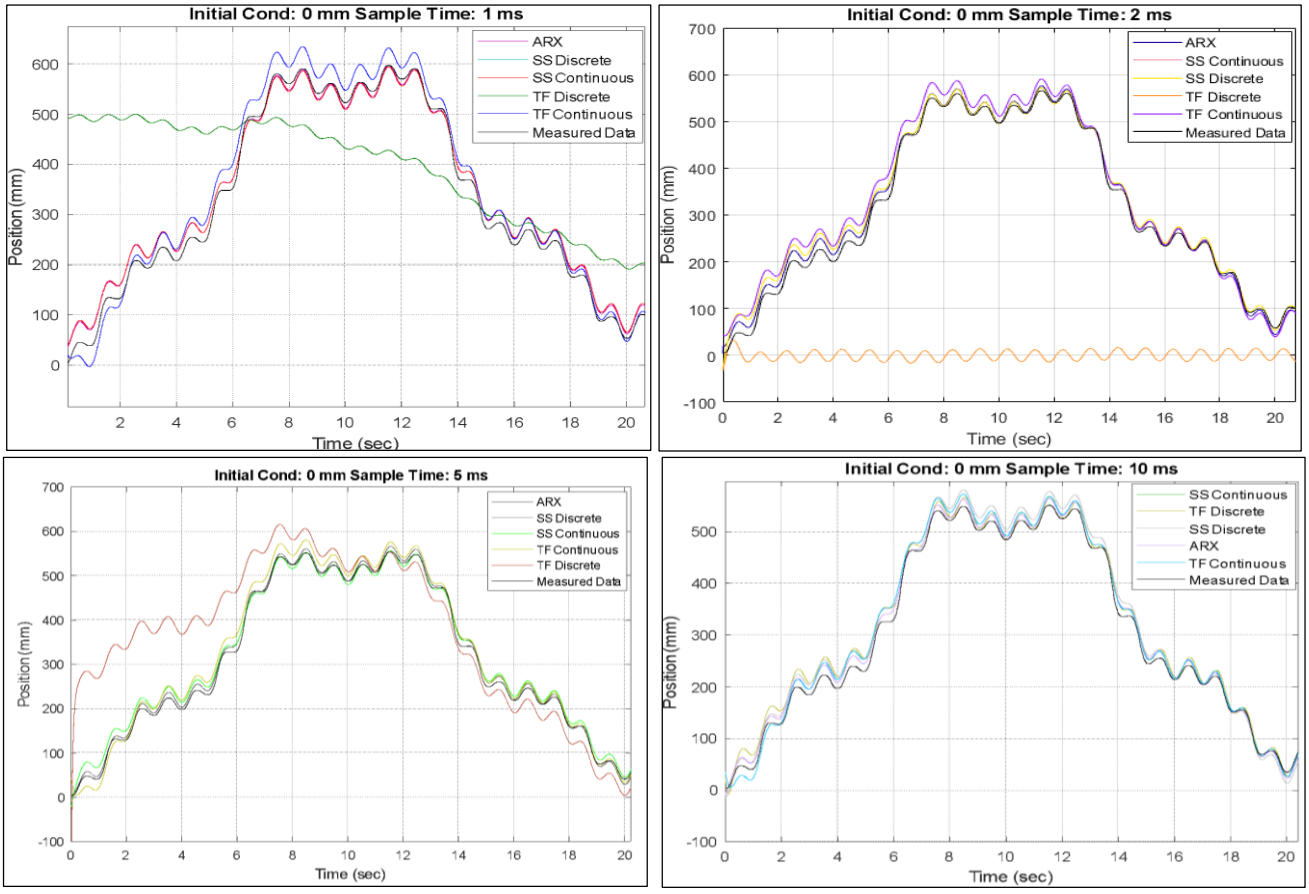

Fig.12. System identification results for 0 mm initial condition with 1, 2, 5, and 10 ms sample times.

The validation FIT results indicate that model performance was also evaluated with test data at different sampling times. Specifically, at low sampling times (1 ms), models created using training data maintained high fit ratios during validation, even when tested with high sampling time test data (e.g., 10 ms). For instance, the SS (Continuous) second-order model, trained with 1 ms data and tested with 10 ms data, achieved a 95.72% validation fit. This demonstrates the generalization ability and applicability of continuous models across different sampling times. In conclusion, while the ARX models

demonstrated superior performance in discrete-time systems, continuous-time transfer function and state-space models allowed for a broader representation of linear systems. These findings highlight the necessity of carefully evaluating the performance and generalization capacities of the chosen model structures in relation to specific applications during the modeling process. The performance of the predicted models at 1 ms, 2 ms, 5 ms, and 10 ms sampling times for the 0 mm initial condition was compared to the measured data and presented in Fig. 12. This figure clearly illustrates how the predicted models represent the system dynamics and the impact of sampling time on model performance.

Table 5 presents the prediction and validation performance of different model structures at 1 ms, 2 ms, 5 ms, and 10 ms sampling times for the 120 mm initial condition. Continuous-time models, particularly the TF Continuous and second-order SS Continuous structures, provided high fit ratios across all sampling times.

The TF Continuous model exhibited stable performance with fit ratios ranging from 94.92% to 96.61%, demonstrating consistent results from low to high sampling times. The SS Continuous models, especially the second-order structure, provided successful results (e.g., 90.62% fit at 10 ms), while the increased complexity of the third-order model negatively impacted validation performance.

Among the discrete-time models, the ARX (4,4,1) model delivered the highest fit ratios and best represented the system dynamics with results ranging from 94.06% to 96.94%. The ARX models demonstrated consistently high performance, not only with training data but also in validation tests. For instance, the ARX (4,4,1) model trained with 5 ms data achieved a fit ratio of 92.67% when validated with 10 ms data. In contrast, TF Discrete models failed to represent the system dynamics, yielding negative fit ratios. This is due to the insufficient representation of information caused by the low sampling frequency in discrete-time TF models.

Validation data analysis shows that continuous-time models maintained their generalization capacity across different sampling times. For example, the TF Continuous model trained with 1 ms data achieved a fit ratio of 89.33% when validated with 10 ms data. Similarly, SS Continuous models exhibited high validation fit at low sampling times, but a decrease in validation performance was observed with the third-order structure.

Table 6 presents the model prediction and validation results conducted under the initial condition of 240 mm. Among the continuous-time models, the TF Continuous and SS Continuous models have stood out. Especially the 3rd degree SS Continuous model has successfully represented the system's dynamics with high accuracy rates. For example, this model, trained with a 5 ms sampling time, achieved a 96.14% fit rate and reached up to 97.12% in validation tests.

The TF Continuous model also achieved satisfactory results in terms of generalization ability, but its accuracy rates were lower compared to the SS Continuous model. Among the discrete-time models, the ARX (4,4,1) model has provided the highest fit rates and has stood out as the structure that best represents the system dynamics with results reaching 97.77%. ARX models have also maintained their generalization capacity in validation tests and have demonstrated stable performance at all sampling times. For example, the ARX (4,4,1) model trained with a 5 ms sampling time achieved a 97.6% fit rate in the 10 ms validation test. In contrast, the TF Discrete models have shown low performance and generally yielded inadequate results in validation tests. At low sampling times (1 ms and 2 ms), both continuous and discrete-time models achieved higher accuracy rates, indicating that low sampling times better capture the detailed dynamic behaviors of the system.

Continuous-time models have reliably represented system dynamics, especially at longer sampling times, while maintaining their generalization capacity. ARX models, on the other hand, have provided reliable results under all test conditions with high accuracy and generalization capacity in discrete-time systems. These analyses reveal that the ARX (4,4,1) model, the 3rd degree SS Continuous model, and the TF Continuous model are the structures that best represent the system dynamics. While the ARX model stands out as a strong option for discrete-time control applications, continuous-time models allow for a broader range of analysis and control of the system. These models provide a suitable foundation for further testing with different types of signals.

The ARX (4,4,1) model has provided the best results for discrete-time systems under both 0 mm and 240 mm initial conditions. This model is a strong option for digital control applications. The TF Continuous model has provided the best result under the initial condition of 120 mm and is recommended for continuous-time analysis and control applications. For ARX models, a sampling time of 10 ms is ideal in terms of both prediction and validation performance. For continuous-time TF models, lower sampling times (e.g., 1 ms) provide higher accuracy.

Among the models evaluated under different initial conditions and sampling intervals, the best-performing structures were selected for further comparison. First, the 3-pole, 2-zero continuous-time transfer function model obtained at a 120 mm initial condition and a 1 ms sampling interval (as shown in Equation 15) was preferred due to its high fit rate (96.31%) under low sampling intervals and its stable performance during the validation phase.

$$G_1 = \frac{86.48\,s^2 + 845.1s + 9902}{s^3 + 13.99s^2 + 128.9s + 0.7653} \tag{15}$$

Secondly, the ARX(4,4,1) model shown in Equation 16—obtained under a 240 mm initial condition and a 10 ms sampling interval—was chosen for its high prediction accuracy (97.77%) and strong generalization capability.

$$G_2 = \begin{cases} A(z) = 1 - 1.079z^{-1} - 0.2649z^{-2} + 0.07386z^{-3} - 0.4173z^{-4} \\ B(z) = 45.6z^{-1} - 134z^{-2} + 132.2z^{-3} - 43.8z^{-4} \end{cases} \tag{16}$$

Finally, the second-order continuous-time state-space model shown in Equation 17, obtained under the 0 mm initial condition and a 5 ms sampling interval, was preferred due to its low complexity and consistent performance (93.19%) demonstrated during the validation phase.

$$G_3 = \begin{cases} A = \begin{bmatrix} 0.003973 & -0.08541 \\ 0.1342 & -8.391 \end{bmatrix}, \; B = \begin{bmatrix} 0.001494 \\ -0.04018 \end{bmatrix} \\ C = [3.326e+4 \quad -1.065], \quad D = [0] \end{cases} \tag{17}$$

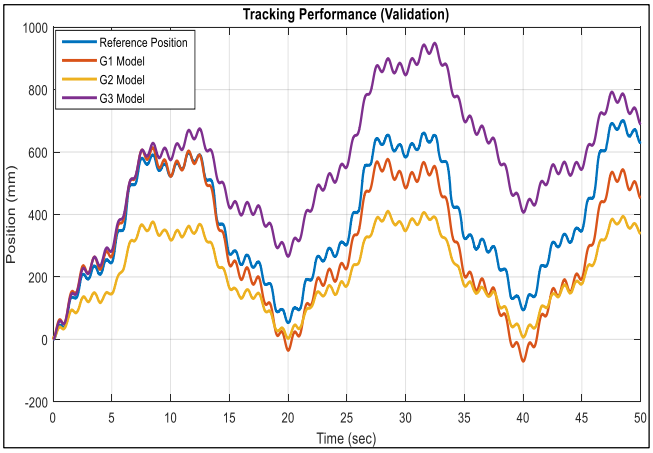

Fig. 13. Tracking performance during the validation phase for different models (G_1, G_2, G_3).

The performance of the system models was further evaluated using three commonly used error metrics: Root Mean Square Error (RMSE), Mean Absolute Error (MAE), and Integral of Time-weighted Absolute Error (ITAE), as shown in Equation 18.

Fig. 14 indicates that the G_1 model exhibits markedly reduced RMSE and MAE values in comparison to G_2 and G_3, suggesting superior tracking accuracy and robustness. Moreover, the ITAE values, which highlight long-term cumulative error, demonstrate that G_1 exhibits enhanced performance with time. (The ITAE values were scaled by a factor of 10^9 for visualization purposes.)

$$RMSE = \sqrt{\frac{1}{N}\sum_{i=1}^{N}(e(t))^2},\ ITAE = \int t|e(t)|dt$$
$$MAE = \frac{1}{N}\sum_{i=1}^{N}|e(t)| \quad (18)$$

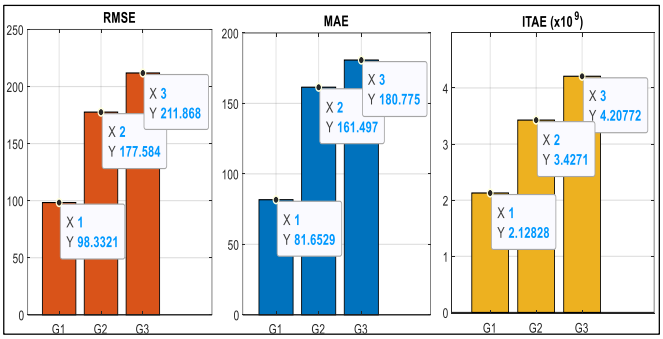

Fig. 14. Tracking error metrics comparison.

TABLE IV
MODEL ESTIMATION AND VALIDATION RESULTS WITH A 0 MM INITIAL CONDITION

Sample Time	Model Type	Model Structure	FIT (%)	Validation FIT 1 ms → 2 ms	Validation FIT 1 ms → 5 ms	Validation FIT 1 ms → 10 ms
1 ms	TF (*Continuous*)	3 pole, 2 zero	85.77	85.71	86.11	87.5
	SS (*Continuous*)	Second-order	88.7	93.83	96.12	95.72
	SS (*Continuous*)	Third-order	NaN	NaN	NaN	NaN
	TF (*Discrete*)	3 pole, 2 zero	-21.98	x	x	x
	SS (*Discrete*)	Second-order	88.7	x	x	x
	SS (*Discrete*)	Third-order	NaN	x	x	x
	ARX (*Discrete*)	(3,3,1)	89.47	x	x	x
	ARX (*Discrete*)	(4,4,1)	92.5	x	x	x
Sample Time	**Model Type**	**Model Structure**	**FIT (%)**	**Validation FIT 2 ms → 1 ms**	**Validation FIT 2 ms → 5 ms**	**Validation FIT 2 ms → 10 ms**
2 ms	TF (*Continuous*)	3 pole, 2 zero	85.3	81.07	87.39	89.49
	SS (*Continuous*)	Second-order	89.95	84.0	92.41	93.81
	SS (*Continuous*)	Third-order	89.96	86.16	91.81	93.36
	TF (*Discrete*)	3 pole, 2 zero	-122.9	x	x	x
	SS (*Discrete*)	Second-order	89.95	x	x	x
	SS (*Discrete*)	Third-order	89.96	x	x	x
	ARX (*Discrete*)	(3,3,1)	93.21	x	x	x
	ARX (*Discrete*)	(4,4,1)	93.4	x	x	x
Sample Time	**Model Type**	**Model Structure**	**FIT (%)**	**Validation FIT 5 ms → 1 ms**	**Validation FIT 5 ms → 2 ms**	**Validation FIT 5 ms → 10 ms**
5 ms	TF (*Continuous*)	3 pole, 2 zero	89.31	84.76	88.23	91.06
	SS (*Continuous*)	Second-order	92.02	83.48	89.64	93.19
	SS (*Continuous*)	Third-order	64.14	59.48	62.12	66.53
	TF (*Discrete*)	3 pole, 2 zero	18.66	x	x	x
	SS (*Discrete*)	Second-order	92.02	x	x	x
	SS (*Discrete*)	Third-order	64.14	x	x	x
	ARX (*Discrete*)	(3,3,1)	95.5	x	x	x
	ARX (*Discrete*)	(4,4,1)	94.92	x	x	x
Sample Time	**Model Type**	**Model Structure**	**FIT (%)**	**Validation FIT 10 ms → 1 ms**	**Validation FIT 10 ms → 2 ms**	**Validation FIT 10 ms → 5 ms**
10 ms	TF (*Continuous*)	3 pole, 2 zero	91.29	84.84	88.43	89.53
	SS (*Continuous*)	Second-order	88.13	81.55	84.31	86.16
	SS (*Continuous*)	Third-order	83.94	75.45	79.47	81.68
	TF (*Discrete*)	3 pole, 2 zero	90.19	x	x	x
	SS (*Discrete*)	Second-order	88.13	x	x	x
	SS (*Discrete*)	Third-order	83.94	x	x	x
	ARX (*Discrete*)	(3,3,1)	93.79	x	x	x
	ARX (*Discrete*)	(4,4,1)	92.49	x	x	x

TABLE V
MODEL ESTIMATION AND VALIDATION RESULTS WITH A 120 MM INITIAL CONDITION

Sample Time	Model Type	Model Structure	FIT (%)	Validation FIT 1 ms → 2 ms	Validation FIT 1 ms → 5 ms	Validation FIT 1 ms → 10 ms
1 ms	TF (*Continuous*)	3 pole, 2 zero	96.31	90.7	89.63	89.33
	SS (*Continuous*)	Second-order	NaN	NaN	NaN	NaN
	SS (*Continuous*)	Third-order	75.36	74.96	76.6	76.89
	TF (*Discrete*)	3 pole, 2 zero	-126	x	x	x
	ARX (*Discrete*)	(3,3,1)	90.68	x	x	x
	ARX (*Discrete*)	(4,4,1)	94.06	x	x	x
Sample Time	**Model Type**	**Model Structure**	**FIT (%)**	**Validation FIT 2 ms → 1 ms**	**Validation FIT 2 ms → 5 ms**	**Validation FIT 2 ms → 10 ms**
2 ms	TF (*Continuous*)	3 pole, 2 zero	95.16	91.62	95.86	95.57
	SS (*Continuous*)	Second-order	NaN	NaN	NaN	NaN
	SS (*Continuous*)	Third-order	67.32	71.6	65.36	64.85
	TF (*Discrete*)	3 pole, 2 zero	-138.7	x	x	x
	ARX (*Discrete*)	(3,3,1)	94.88	x	x	x
	ARX (*Discrete*)	(4,4,1)	95.21	x	x	x
Sample Time	**Model Type**	**Model Structure**	**FIT (%)**	**Validation FIT 5 ms → 1 ms**	**Validation FIT 5 ms → 2 ms**	**Validation FIT 5 ms → 10 ms**
5 ms	TF (*Continuous*)	3 pole, 2 zero	94.92	90.94	93.27	95.04
	SS (*Continuous*)	Second-order	93.73	86.85	92.35	93.55
	SS (*Continuous*)	Third-order	82.41	83.16	82.72	82.18
	TF (*Discrete*)	3 pole, 2 zero	-48.64	x	x	x
	ARX (*Discrete*)	(3,3,1)	96.99	x	x	x
	ARX (*Discrete*)	(4,4,1)	96.64	x	x	x
Sample Time	**Model Type**	**Model Structure**	**FIT (%)**	**Validation FIT 10 ms → 1 ms**	**Validation FIT 10 ms → 2 ms**	**Validation FIT 10 ms → 5 ms**
10 ms	TF (*Continuous*)	3 pole, 2 zero	96.61	93.26	94.46	96.58
	SS (*Continuous*)	Second-order	90.62	93.47	92.02	91.05
	SS (*Continuous*)	Third-order	90.05	90.65	91.55	90.55
	TF (*Discrete*)	3 pole, 2 zero	40.02	x	x	x
	ARX (*Discrete*)	(3,3,1)	95.36	x	x	x
	ARX (*Discrete*)	(4,4,1)	92.67	x	x	x

TABLE VI
MODEL ESTIMATION AND VALIDATION RESULTS WITH A 240 MM INITIAL CONDITION

Sample Time	Model Type	Model Structure	FIT (%)	Validation FIT 1 ms → 2 ms	Validation FIT 1 ms → 5 ms	Validation FIT 1 ms → 10 ms
1 ms	TF (*Continuous*)	3 pole, 2 zero	77	74.67	75.04	76.36
	SS (*Continuous*)	Second-order	89.03	94.55	95.15	93.06
	SS (*Continuous*)	Third-order	95.63	91.16	89.7	88.3
	TF (*Discrete*)	3 pole, 2 zero	76.36	x	x	x
	ARX (*Discrete*)	(3,3,1)	89.69	x	x	x
	ARX (*Discrete*)	(4,4,1)	91.87	x	x	x
Sample Time	**Model Type**	**Model Structure**	**FIT (%)**	**Validation FIT 2 ms → 1 ms**	**Validation FIT 2 ms → 5 ms**	**Validation FIT 2 ms → 10 ms**
2 ms	TF (*Continuous*)	3 pole, 2 zero	87.69	84.1	88.43	89.68
	SS (*Continuous*)	Second-order	90.82	83.33	93.51	93.53
	SS (*Continuous*)	Third-order	93.91	88.12	96.52	96.69
	TF (*Discrete*)	3 pole, 2 zero	80.4	x	x	x
	ARX (*Discrete*)	(3,3,1)	93.65	x	x	x
	ARX (*Discrete*)	(4,4,1)	95.1	x	x	x
Sample Time	**Model Type**	**Model Structure**	**FIT (%)**	**Validation FIT 5 ms → 1 ms**	**Validation FIT 5 ms → 2 ms**	**Validation FIT 5 ms → 10 ms**
5 ms	TF (*Continuous*)	3 pole, 2 zero	87.55	82.84	86.1	88.95
	SS (*Continuous*)	Second-order	93.34	83.39	90.81	93.17
	SS (*Continuous*)	Third-order	96.14	86.9	93.03	97.12
	TF (*Discrete*)	3 pole, 2 zero	68.05	x	x	x
	ARX (*Discrete*)	(3,3,1)	97.65	x	x	x
	ARX (*Discrete*)	(4,4,1)	97.6	x	x	x
Sample Time	**Model Type**	**Model Structure**	**FIT (%)**	**Validation FIT 10 ms → 1 ms**	**Validation FIT 10 ms → 2 ms**	**Validation FIT 10 ms → 5 ms**
10 ms	TF (*Continuous*)	3 pole, 2 zero	89.57	82.72	86.82	88.12
	SS (*Continuous*)	Second-order	95.48	86.17	91.14	93.8
	SS (*Continuous*)	Third-order	94.81	89.59	95.34	96.74
	TF (*Discrete*)	3 pole, 2 zero	11.67	x	x	x
	ARX (*Discrete*)	(3,3,1)	97.57	x	x	x
	ARX (*Discrete*)	(4,4,1)	97.77	x	x	x

 ISSN: 2147-284X http://dergipark.gov.tr/bajece

B. Real-Time Control Implementation

Among the models identified using different structures and sampling times, the one referred to as G_1, which exhibited the lowest tracking error during addition test, was selected for control application. This model provided the most accurate dynamic representation of the EHS and was thus integrated into the closed-loop control design. Based on the G_1 system model, the sampling time and controller configuration were determined for real time application.

For the control of the EHS, a Proportional-Integral (PI) controller was employed. A control interface was developed in LabVIEW to apply voltage signals in the range of –10 V to +10 V to the proportional directional control valve. Various signal types (e.g., sine, square, and step) could be generated for reference tracking. The measured position of the hydraulic cylinder was continuously compared with the desired position command, and the resulting position error was used to compute the control input. The most appropriate cycle time for the control loop was selected based on the previously identified system dynamics.

The use of PI controllers in hydraulic systems offers significant advantages in terms of maintaining equilibrium and enhancing system response. By combining proportional and integral components, the PI controller delivers both immediate reactions to system deviations and corrections based on historical errors. The *P* term in PI control refers to the control mechanism that responds rapidly in proportion to the error between the desired and measured positions. In this study, this response was executed via a proportional directional control valve, which quickly intervenes in system deviations to make instantaneous corrections. The *I* term in PI control, on the other hand, represents the accumulation of error. It attempts to compensate for constant imbalances in the system (such as friction, leakage, or unmodeled dynamics) based on errors accumulated over time. If a persistent error exists, the integral component integrates this error and sends additional corrective signals to the proportional directional control valve, thereby eliminating permanent discrepancies in the system. By combining these two terms, the PI controller ensures that the EHS operates more precisely, stably, and reliably.

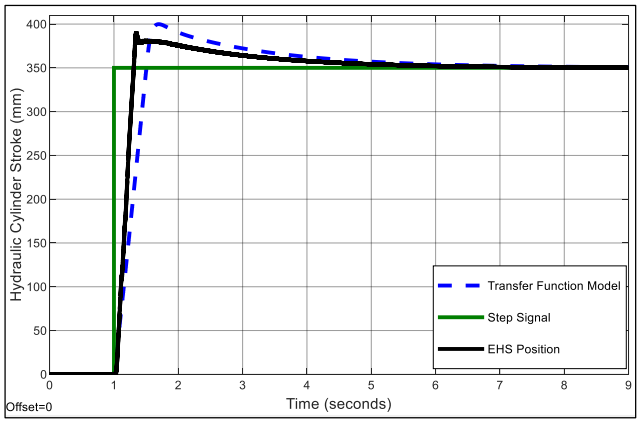

Fig. 15. Transfer function model and EHS position graphs (Green: step signal; Black: EHS position; Blue: transfer function model position).

In this study, since the model of the EHS provided the transfer function with the highest accuracy and fidelity, the determination of the PI parameters was carried out within a MATLAB/Simulink simulation environment and subsequently applied to the EHS. The PI controller parameters for the control of the EHS were determined based on the model developed in the Simulink environment. Initially, the proportional gain K_p and integral gain K_i were both set to 0, and the system response was observed. Subsequently, the K_p and K_i values were gradually increased to optimize the behavior of the closed-loop system. During the simulation process, the accuracy and stability of the EHS position control were analyzed, and the optimal values were determined as K_p = 0.28 and K_i = 0.14. These parameters were then integrated into the LabVIEW software and implemented in the system. As a result, it was verified that the PI controller successfully adapted to the dynamic characteristics of the EHS and effectively achieved the desired position control.

A LabVIEW control loop speed of 1 ms was employed when implementing the PI controller coefficients on the EHS and generating the desired step signal. Figure 15 presents the system's closed-loop response under PI control, showing the actual EHS position, the applied step reference signal, and the theoretical response predicted by the identified transfer function model. This model, derived from the system identification process, was used in the MATLAB/Simulink environment for tuning the controller parameters. The close agreement between the real system response and the model output verifies both the effectiveness of the PI controller and the accuracy of the identified model used in the control design.

IV. Conclusion and Discussion

This study comprehensively examined the dynamics of an EHS in a laboratory-scale wave channel using black-box modeling and advanced control techniques. Utilizing the SIT in MATLAB/Simulink, various model structures—including continuous-time transfer functions, state-space models, and discrete-time ARX models—were developed and evaluated under different initial conditions and sampling times. According to comparative simulation results, a third-order continuous-time transfer function was identified as the most suitable model structure. Since responses were obtained from the transfer function model with a 1-millisecond cycle time, the control program in LabVIEW was also set to a 1-ms cycle time for the controller.

Additionally, based on the most accurate model obtained, a PI controller was implemented for EHS position control using LabVIEW. The controller parameters were optimized in the MATLAB/Simulink environment, with the proportional gain K_p set to 0.28 and the integral gain K_i set to 0.14. The integration of this PI controller into the system provided significant improvements in tracking performance and system stability by rapidly responding to instantaneous deviations and accounting for accumulated errors. Overall, the findings of this study highlight the critical importance of accurate system identification in enhancing the performance of electro-hydraulic systems in wave generation. The selected modeling approaches and control strategies improve the predictability and reliability of such systems, providing a robust foundation for future research.

Although the developed models and the PI control implementation yielded promising results, the study focused on a specific system configuration and controlled operating conditions. Factors such as external disturbances, strong nonlinearities beyond the tested range, and long-term operational behavior were not within the scope of this work. Future research may explore advanced nonlinear identification techniques—such as neural networks or hybrid

grey-box models—to better capture complex dynamics, and validate the approach under broader operating scenarios to improve generalizability.

REFERENCES

[1] M. Özbulut, "Düzenli Dalgalar Üreten Bir Sayısal Dalga Tankının SPH Yöntemi ile Modellenmesi," Uludağ University Journal of The Faculty of Engineering, pp. 551–570, Sep. 2019, doi: 10.17482/uumfd.509229.

[2] M. A. Drzewiecki and J. Guzinski, "Application of the ISE Optimized Proportional Control of the Wave Maker in a Towing Tank," IEEE Access, vol. 10, pp. 42151–42162, 2022, doi: 10.1109/ACCESS.2022.3168047.

[3] S. Mahjouri, R. Shabani, G. Rezazadeh, and P. Badiei, "Active Control of A Piston-Type Absorbing Wavemaker with Fully Reflective Structure," China Ocean Engineering, vol. 34, no. 5, pp. 730–737, Sep. 2020, doi: 10.1007/s13344-020-0066-9.

[4] Y. Liu, Y. Zheng, R. Song, J. Chen, and H. Jin, "Wave generation characteristic analysis of piston and flap type wave maker with rotary-valve-control vibrator," Journal of Vibration and Control, vol. 26, no. 15–16, pp. 1297–1308, Aug. 2020, doi: 10.1177/1077546319895664.

[5] B. Nouioui and M. Doğan, "Irregular Wavemaker (Piston Type) in a Numerical and Physical Wave Tank," Usak University Journal of Engineering Sciences, vol. 5, no. 2, pp. 95–116, Dec. 2022, doi: 10.47137/uujes.1180866.

[6] M. Y. Coşkun and M. İtik, "Reinforcement learning based position control of an electro-hydraulic system," Niğde Ömer Halisdemir University Journal of Engineering Sciences, vol. 12, no. 1, pp. 280–288, 2023, doi: 10.28948/ngmuh.1163241.

[7] H. U. Akova and T. Balkan, "Elektro-Hidrolik Yük Simülatörü İçin Geribesleme Doğrusallaştırma Yöntemi ile Kuvvet Kontrolü Tasarımı," in *Proceedings of the VIII. Ulusal Hidrolik Pnömatik Kongresi*, Istanbul, Türkiye, 2012, pp. 295–306.

[8] Rahmat, "Modeling and Controller Design of an Electro-Hydraulic Actuator System," Am J Appl Sci, vol. 7, no. 8, pp. 1100–1108, Aug. 2010, doi: 10.3844/ajassp.2010.1100.1108.

[9] M. F. Rahmat, S. Rozali, A. Wahab, and Zulfatman, "Application Of Draw Wire Sensor In Position Tracking Of Electro Hydraulic Actuator System," *International Journal on Smart Sensing and Intelligent Systems*, vol. 3, no. 4, pp. 736-755, 2010.

[10] Y. Lin, Y. Shi, and R. Burton, "Modeling and Robust Discrete-Time Sliding-Mode Control Design for a Fluid Power Electrohydraulic Actuator (EHA) System," IEEE/ASME Transactions on Mechatronics, vol. 18, no. 1, pp. 1–10, Feb. 2013, doi: 10.1109/TMECH.2011.2160959.

[11] J. Das, S. Kr. Mishra, R. Saha, S. Mookherjee, and D. Sanyal, "Nonlinear modeling of an electrohydraulic actuation system via experiments and its characterization by means of neural network," Journal of the Brazilian Society of Mechanical Sciences and Engineering, vol. 40, no. 2, p. 58, Feb. 2018, doi: 10.1007/s40430-018-0979-x.

[12] S. Salleh, M. F. Rahmat, S. M. Othman, and H. Z. Abidin, "Application of Draw Wire Sensor in the Tracking Control of an Electro-Hydraulic Actuator System," *Journal of Technology*, vol. 73, no. 6, pp. 51–57, 2015.

[13] R. Ghazali, M. Sam, M. F. Rahmat, K. Jusoff, Zulfatman, and A. Hashim, "Self-Tuning Control of an Electro-Hydraulic Actuator System," *International Journal on Smart Sensing and Intelligent Systems*, vol. 4, no. 2, pp. 189-204, 2011.

[14] J. Yan, B. Li, H.-F. Ling, H.-S. Chen, and M.-J. Zhang, "Nonlinear State Space Modeling and System Identification for Electrohydraulic Control," Math Probl Eng, vol. 2013, pp. 1–9, 2013, doi: 10.1155/2013/973903.

[15] S. Kizir, T. Yaren, and E. Kelekçi, Matlab Simulink Destekli Gerçek Zamanlı Kontrol: Teori ve Mühendislik Uygulamaları. Ankara, Türkiye: Seçkin Yayıncılık, 2019.

[16] L. Jin and Q. Wang, "Accurate model identification of the inertial mass dynamic of hydraulic cylinder with model uncertainty," Proceedings of the Institution of Mechanical Engineers, Part I: Journal of Systems and Control Engineering, vol. 233, no. 5, pp. 501–510, May 2019, doi: 10.1177/0959651818802113.

[17] A. Mitov, T. Slavov, and J. Kralev, "Robustness Analysis of an Electrohydraulic Steering Control System Based on the Estimated Uncertainty Model," Information, vol. 12, no. 12, p. 512, Dec. 2021, doi: 10.3390/info12120512.

[18] A. Mitov, J. Kralev, T. Slavov, and I. Angelov, "Comparison of Model Predictive Control (MPC) and Linear-Quadratic Gaussian (LQG) Algorithm for Electrohydraulic Steering Control System," E3S Web of Conferences, vol. 207, p. 04001, Nov. 2020, doi: 10.1051/e3sconf/202020704001.

[19] B. Yu, Q. Zhu, J. Yao, J. Zhang, Z. Huang, Z. Jin, and X. Wang, "Design, mathematical modeling and force control for electro-hydraulic servo system with pump-valve compound drive," *IEEE Access*, vol. 8, pp. 171988–172003, 2020, doi: 10.1109/ACCESS.2020.3012091.

[20] J. Zhao, D. Song, B. Zhu, Z. Chen, and Y. Sun, "Nonlinear Backstepping Control of Electro-Hydraulic Brake System Based on Bond Graph Model," *IEEE Access*, vol. 8, pp. 19100–19112, Jan. 2020, doi: 10.1109/ACCESS.2020.2968513.

[21] J. Schwarz and B. Lohmann, "Robust identification and control of mobile hydraulic systems using a decentralized valve structure," Control Engineering Practice, vol. 151, Art. no. 106030, 2024. Available: https://doi.org/10.1016/j.conengprac.2024.106030.

[22] A. He, L. Wei, Q. Lu, and P. He, "An Investigation of Energy Consumption Characteristics of the Pump-Control System for Electric Excavator Arms," Applied Sciences, vol. 14, no. 23, Art. no. 10791, Nov. 2024. doi: 10.3390/app142310791.

[23] S. Han, G. Orzechowski, J.-G. Kim, and A. Mikkola, "Data-driven friction force prediction model for hydraulic actuators using deep neural networks," Mechanism and Machine Theory, vol. 192, Art. no. 105545, 2024. doi: 10.1016/j.mechmachtheory.2023.105545.

[24] S.-W. Kim, B. Cho, S. Shin, J.-H. Oh, J. Hwangbo, and H.-W. Park, "Force Control of a Hydraulic Actuator With a Neural Network Inverse Model," IEEE Robotics and Automation Letters, vol. 6, no. 2, pp. 2814–2821, Apr. 2021, doi: 10.1109/LRA.2021.3062353.

[25] S. Jiang, H. Wang, and G. Zhao, "Research on neural network model reference adaptive disturbance rejection control of digital hydraulic cylinder," Advances in Mechanical Engineering, vol. 14, no. 12, pp. 1–15, 2022, doi: 10.1177/16878132221140706.

[26] R. Dindorf, "Dynamic Modeling and Simulation of a Discrete Incremental Hydraulic Positioning System Controlled by Binary Valves," Applied Sciences, vol. 14, no. 7, Art. no. 2973, Apr. 2024. doi: 10.3390/app14072973.

[27] National Instruments Corp., "cRIO-9074 - NI." Accessed: Jul. 20, 2024. [Online]. Available: https://www.ni.com/en-tr/support/model.crio-9074.html

BIOGRAPHIES

Batin Demircan graduated with a B.Sc. degree in electrical and electronics engineering from the Kirikkale University in 2015, M.Sc. degree in electrical and electronics engineering from the Balikesir University in 2019. Since 2022, he has been an Lecturer and PhD.Candidate with the Electronics and Automation Department, Balikesir Vocational School, Balikesir University, Balikesir. His research interest include control systems, renewable energy systems and IoT distributed systems.

Tugce Yaren graduated with a B.Sc. degree in Mechatronics Engineering in 2014, received her M.Sc. degree in 2018, and completed her Ph.D. in 2024, all from Kocaeli University, Kocaeli, Turkey. From 2016 to 2024, she worked as a Research Assistant in the Department of Mechatronics Engineering at Kocaeli University. Since 2024, she has been serving as an Assistant Professor in the Department of Electrical and Electronics Engineering at Balıkesir University. Her research interests include the modeling of nonlinear systems, real-time control, system dynamics and control (e.g., optimal control, model predictive control), and robotics.

Ersin Akyuz is an Associate Professor at the Department of Electrical and Electronics Engineering, Faculty of Engineering, Balikesir University, Balikesir, Turkey. He graduated from the Istanbul Technical University in 1996. He received his MSc in Gazi University, Department of Electric-Electronic in 2003. He received his PhD in Balikesir University Mechanical Engineering in 2010. His research interests are renewable energy, hydrogen energy, and IoT distributed systems.

Sabri Bicakci was born in Balikesir, Turkey in 1982. He received the B.S. degree in electronics engineering from the Erciyes University, Kayseri, in 2005, M.S. degree in electrical and electronics engineering from the Balikesir University, Balikesir, in 2009 and the Ph. D. degree in mechanical engineering from Balikesir University, Balikesir, in 2012. From 2005 to 2015, he was a Research Assistant with Electrical and Electronics Engineering Department, Balikesir University. Since 2015, he has been an Assistant Professor with the Mechatronics Engineering Department, Balikesir University. His research interest includes robotics and control systems.